

Structural and paramagnetic properties of dilute $\text{Ga}_{1-x}\text{Mn}_x\text{N}$

Wiktor Stefanowicz,^{1,2} Dariusz Sztenkiel,² Bogdan Faina,³ Andreas Grois,³ Mauro Rovezzi,^{3,4} Thibaut Devillers,³ Francesco d’Acapito,⁵ Andrea Navarro-Quezada,³ Tian Li,³ Rafał Jakiela,² Maciej Sawicki,^{2,*} Tomasz Dietl,^{2,6,†} and Alberta Bonanni^{3,‡}

¹Laboratory of Magnetism, Bialystok University, ul. Lipowa 41, 15-424 Bialystok, Poland

²Institute of Physics, Polish Academy of Science, ul. Lotników 32/46, PL-02-668 Warszawa, Poland

³Institut für Halbleiter- und Festkörperphysik, Johannes Kepler University, Altenbergerstr. 69, A-4040 Linz, Austria

⁴Italian Collaborating Research Group, BM08 “GILDA”, ESRF, BP 220, F-38043 Grenoble, France

⁵Consiglio Nazionale delle Ricerche, IOM-OGG, c/o ESRF GILDA CRG, BP 220, F-38043 Grenoble, France

⁶Institute of Theoretical Physics, University of Warsaw, PL-00-681 Warszawa, Poland

(Dated: November 15, 2018)

Systematic investigations of the structural and magnetic properties of single crystal $\text{Ga}_{1-x}\text{Mn}_x\text{N}$ films grown by metal organic vapor phase epitaxy are presented. High resolution transmission electron microscopy, synchrotron x-ray diffraction, and extended x-ray absorption fine structure studies do not reveal any crystallographic phase separation and indicate that Mn occupies Ga-substitutional sites in the Mn concentration range up to 1%. The magnetic properties as a function of temperature, magnetic field and its orientation with respect to the c -axis of the wurtzite structure can be quantitatively described by the paramagnetic theory of an ensemble of non-interacting Mn^{3+} ions in the relevant crystal field, a conclusion consistent with the x-ray absorption near edge structure analysis. A negligible contribution of Mn in the 2+ charge state points to a low concentration of residual donors in the studied films. Studies on modulation doped p -type $\text{Ga}_{1-x}\text{Mn}_x\text{N}/(\text{Ga},\text{Al})\text{N}:\text{Mg}$ heterostructures do not reproduce the high temperature robust ferromagnetism reported recently for this system.

PACS numbers: 75.50.Pp, 75.10.Dg, 75.70.Ak, 75.30.Gw, 81.05.Ea

I. INTRODUCTION

The search for magnetic semiconductors with a Curie temperature T_C above room temperature (RT) is currently one of the major challenges in semiconductor spintronics.^{1–3} In single-phase samples the highest Curie temperatures reported are ~ 190 K for $(\text{Ga},\text{Mn})\text{As}$.^{4,5} The magnetic ordering in these materials is interpreted in terms of the $p-d$ Zener model.^{1,6} This model assumes that dilute magnetic semiconductors (DMSs) are random alloys, where a fraction of the host cations is substitutionally replaced by magnetic ions – hereafter with magnetic ions we intend transition metal ions – and the indirect magnetic coupling is provided by delocalized or weakly localized carriers ($sp-d$ exchange interactions). The authors adopted the Zener approach within the virtual-crystal (VCA) and molecular-field (MFA) approximations with a proper description of the valence band structure in zinc-blende and wurtzite (wz) DMSs. The model takes into account the strong spin-orbit and the $k \cdot p$ couplings in the valence band as well as the influence of strain on the band density of states. This approach describes qualitatively, and often quantitatively the thermodynamic, micromagnetic, transport, and spectroscopic properties of DMSs with delocalized holes.^{3,7}

Experimental data for $\text{Ga}_{1-x}\text{Mn}_x\text{N}$ reveal an astonishingly wide spectrum of magnetic properties: some groups find high temperature ferromagnetism^{8–10} with T_C up to 940 K,¹⁰ however other detect only a paramagnetic response and their results show that the spin–spin coupling

is dominated by antiferromagnetic interactions. Generally, the origin of the ferromagnetic response in Mn doped GaN is not clear and two basic approaches to this issue have emerged, namely: i) methods based on the mean-field Zener model.¹ – according to this insight, in the absence of delocalized or weakly localized holes, no ferromagnetism is expected for randomly distributed diluted spins. Indeed, recent studies of $(\text{Ga},\text{Mn})\text{N}$ indicate that in samples containing up to 6% of diluted Mn, holes are strongly localized and, accordingly, T_C below 10 K is experimentally revealed.^{11,12} Higher values of T_C could be obtained providing that efficient methods of hole doping will be elaborated for nitride DMSs. Surprisingly, however, electric field controlled RT ferromagnetism has been recently reported in $\text{Ga}_{1-x}\text{Mn}_x\text{N}$ layers, with a Mn content as low as $x \approx 0.25\%$.¹³ These results ($T_C \gtrsim 300$ K) cannot be explained in the context of the $p-d$ Zener model, where the Curie temperature increases linearly with the Mn concentration and for $x < 0.5\%$ T_C should not exceed 60 K; ii) several studies^{14–16} acknowledge the (likely) presence of secondary phases – originating from the low solubility of magnetic ions in GaN – as being responsible for the observation of ferromagnetism. It has been found that the aggregation of magnetic ions leads either to crystallographic phase separation, i.e., to the precipitation of a magnetic compound, nanoclusters of an elemental ferromagnet, or to the chemical phase separation into regions with respectively high and low concentration of magnetic cations, formed without distortion of the crystallographic struc-

ture. It has been proposed recently that the aggregation of magnetic ions can be controlled by varying their valence (i.e. by tuning the Fermi level). Particularly relevant in this context are data for (Zn,Cr)Te,¹⁷ (Ga,Fe)N,¹⁸ and also (Ga,Mn)N,^{17,19,20} where a strict correlation between codoping, magnetic properties, and magnetic ion distribution has been put into evidence.

There is generally a close relation between the ion arrangement and the magnetic response of a magnetically doped semiconductor. Specifically, depending on different preparation techniques and parameters, coherently embedded magnetic nanocrystals [like wz-MnN in GaN (Refs. 21 and 22)] or precipitates [like *e.g.* MnGa or Mn₄N] might in fact give the major contribution to the total magnetic moment of the investigated samples. In particular, randomly distributed localized spins may account for the paramagnetic component of the magnetization, whereas regions with a high local density of magnetic cations are presumably responsible for ferromagnetic features.²³ In the case of low concentrations of the magnetic impurity, it is often exceedingly challenging to categorically identify the origin of the ferromagnetic signatures.

Up to very recently, in most of the reports the observation of ferromagnetism or ferromagnetic-like behavior with apparent Curie temperatures near or above RT, has been discussed primarily or even solely based on magnetic hysteresis measurements. However, indirect means like superconducting quantum interference device (SQUID) magnetometry measurements or even the presence of the anomalous or extraordinary Hall effect, may be not sufficient for a conclusive statement and to verify a single-phase system. Therefore, a careful and thorough characterization of the systems at the nanoscale is required. This can only be achieved through a precise correlation of the measured magnetic properties with advanced material characterization methods, like *e.g.* synchrotron x-ray diffraction (SXRD), synchrotron based extended x-ray absorption fine structure (EXAFS) and advanced element-specific microscopy techniques, suitable for the detection of a crystallographic and/or chemical phase separation.

The present work is devoted to a comprehensive study of the Ga_{1-x}Mn_xN ($x \leq 1\%$) fabricated by metalorganic vapor phase epitaxy (MOVPE), which was also employed by other authors.^{13,19} A careful on-line control of the growth process is carried out, which is followed by an extended investigation of the structural, optical, and magnetic properties in order to shed new light onto the mechanisms responsible for the magnetic response of the considered system. Particular attention is devoted to avoid the contamination of the SQUID magnetometry signal with spurious effects and, thus, to the reliable determination of the magnetic properties. Experimental procedures involving SXRD, high resolution transmission electron microscopy (HRTEM), EXAFS and x-ray absorption near-edge spectroscopy (XANES) are employed to probe the possible presence of secondary phases, pre-

cipitates or nanoclusters, as well as the chemical phase separation. Moreover, we extensively analyze the properties of single magnetic-impurity states in the nitride host. The understanding of this limit is crucial when considering the most recent suggestions for the controlled incorporation of the magnetic ions and consequently of the magnetic response through Fermi level engineering. By combining the different complementary characterization techniques we establish that randomly distributed Mn ions with a concentration $x < 1\%$ generate a paramagnetic response down to at least 2 K in Ga_{1-x}Mn_xN. In view of our findings, the room temperature ferromagnetism observed in this Mn concentration range^{13,19,20,24,25} has to be assigned to a non-random distribution of transition metal impurities in GaN. We emphasize that in all reported works on (Ga,Mn)N fabricated by MOVPE the Mn concentration was well below 5%.

The paper is organized as follows: in the next section we give a summary of the fabrication details, *in situ* monitoring of the employed MOVPE process and an abridged overview of the characterization techniques, together with a table listing the principal properties and parameters characterizing the (Ga,Mn)N-based samples considered. In Sec. IV the results of the structural analysis of the layers by SXRD, HRTEM, and EXAFS are reported. These measurements prove a uniform distribution of the Mn ions in the Ga sublattice of GaN. Section V is devoted to the determination of the Mn concentration and of the charge and electronic state of the magnetic ions. In section VI we give the experimental magnetization characteristics of the system obtained from SQUID measurements, and interpret the data based on the group theoretical model for Mn³⁺ ions taking into account the trigonal crystal field, the Jahn-Teller distortion and the spin-orbit coupling. Finally, conclusions and outlook stemming from our work are summarized in Sec. VII.

II. GROWTH PROCEDURE

The wz-(Ga,Mn)N epilayers here considered are fabricated by MOVPE in an AIXTRON 200 RF horizontal reactor. All structures have been deposited on *c*-plane sapphire substrates with TMGa (trimethylgallium), NH₃, and MeCp₂Mn (bis-methylcyclopentadienyl-manganese) as precursors for, respectively, Ga, N and Mn, and with H₂ as carrier gas. The growth process has been carried out according to a well established procedure²⁶ consisting of: substrate nitridation, low temperature (540°C) deposition of a GaN nucleation layer (NL), annealing of the NL under NH₃ until recrystallization and the growth of a $\sim 1 \mu\text{m}$ thick device-quality GaN buffer at 1030°C. On top of these structures, Mn doped GaN layers (200-700 nm) at 850°C, at constant TMGa and different—over the samples series—MeCp₂Mn flow-rates ranging from 25 to 490 sccm (standard cubic centimeters per minute) have

TABLE I: Data related to the investigated $\text{Ga}_{1-x}\text{Mn}_x\text{N}$. The following values are listed: the MeCp_2Mn flow rate employed to grow the Mn-doped layers, the FWHM of the (0002) reflex from GaN determined by *ex situ* HRXRD, the Mn^{3+} concentration as obtained from magnetization data, the total Mn content from SIMS measurements and the thickness of each (Ga,Mn)N layer. Letters A and B denote the two different growth series

sample number	MeMnCp ₂ flow rate [sccm]	thickness of (Ga,Mn)N [nm]	FWHM [arcsec]	Mn ³⁺ conc. SQUID [10 ²⁰ cm ⁻³]	Mn conc. SIMS [10 ²⁰ cm ⁻³]
000B	0	470		<0.06	
025A	25	450	242	0.28	0.3
050A	50	400	267	0.8	0.6
100A	100	400	243	0.8	
100B	100	520		0.27	
125A	125	400	267	0.6	0.5
150A	150	400	247	1.0	0.7
175A	175	400	251	2.2	
200B	200	500		0.9	
225A	225	370	263	1.6	1.1
250A	250	370	243	1.4	
275A	275	400	256	1.6	
300A	300	400	272	1.4	1.3
300B	300	520		1.4	
325A	325	400	269	2.2	
350A	350	370	273	2.2	
375A	375	400	284	2.5	1.9
400A	400	370	265	2.6	
400B	400	500		2.0	
475A	475	700		2.7	
490A	490	700		3.8	2.4
490B	490	470		2.7	

been grown. The nominal Mn content in subsequently grown samples has been alternatively switched from low to high and, *vice versa*, to minimize long term memory effects due to the presence of residual Mn in the reactor. During the whole growth process the samples have been continuously rotated in order to promote the deposition homogeneity and *in situ* and on line ellipsometry is employed for the real time control over the entire fabrication process. The p-type superlattices have been grown according to the optimized procedure already reported.²⁷ Our MOVPE system is equipped with an *in situ* Isa Jobin Yvon ellipsometer that allows both spectroscopic (variation of the optical parameters as a function of the radiation wavelength) and kinetic (ellipsometric angles *vs.* time) measurements^{28,29} in the energy range 1.5 - 5.5 eV. In Table I the considered (Ga,Mn)N samples are listed together with their specific parameters.

III. EXPERIMENTAL TECHNIQUES

A. HRTEM experimental

HRTEM studies have been carried out on cross-sectional samples prepared by standard mechanical polishing followed by Ar⁺ ion milling, under a 4° angle at 4 kV for less than 2 h. The ion polishing has been performed in a Gatan 691 PIPS system. The specimens were investigated using a JEOL 2011 Fast TEM micro-

scope operated at 200 kV equipped with a Gatan CCD camera. The set-up is capable of an ultimate point-to-point resolution of 0.19 nm, with the possibility to image lattice fringes with a 0.14 nm resolution. The chemical analysis has been accomplished with an Oxford Inca energy dispersive x-ray spectroscopy (EDS) system.

B. HRXRD and SXRD experimental

High-resolution x-ray diffraction (HRXRD) rocking curves are routinely acquired on each sample with a Philips XRD HR1 vertical diffractometer with a CuK_α x-ray source working at a wavelength of 0.15406 nm (\sim 8 keV). A monochromator with a Ge(440) crystal configuration is used to collimate the beam, that is diffracted and collected by a Xe-gas detector. Angular (ω) and radial $\omega/2\theta$ scans have been collected along the growth direction for the (002) GaN reflex, in order to gain information on the crystal quality of the samples from the full width at half maximum (FWHM) of the diffraction peak.

Though being aware that, if great care is exercised, also conventional XRD may allow to detect small embedded clusters (like in the reported case of Co in ZnO)³⁰⁻³² we performed SXRD measurements that gave us the possibility to additionally carry out *in situ* annealing experiments. The experiments have been carried out at the beamline BM20 (Rossendorf Beam Line) of the European Synchrotron Radiation Facility (ESRF) in Grenoble - France. Radial coplanar scans in the 2θ range from 20° to 60° were acquired at a photon energy of 10 keV. The beamline is equipped with a double-crystal Si(111) monochromator with two collimating/focusing mirrors (Si and Pt-coating) for rejection of higher harmonics, allowing an acquisition energy range from 6 to 33 keV. The measurements are performed using a heavy-duty 6-circle Huber diffractometer, that is the system is suitable for (heavy) user-specific environments (*e.g.* in our case a Be-dome for the annealing experiments was required).

C. EXAFS and XANES experimental

The x-ray absorption fine structure (XAFS) measurements at the Mn-K edge (6539 eV) have been performed at the GILDA Italian collaborating research group beamline (BM08) of the ESRF in Grenoble.³³ The monochromator is equipped with a pair of Si(311) crystals and run in dynamical focusing mode.³⁴ Harmonics rejection is achieved through a pair of Pd-coated mirrors with an estimated cutoff of 18 keV. Data are collected in the fluorescence mode using a 13-element hyper pure Ge detector and normalized by measuring the incident beam with an ion chamber filled with nitrogen gas. In order to minimize the effects of coherent scattering from the substrate, the samples are mounted on a dedicated sample holder for grazing-incidence geometry,³⁵ measurements are car-

ried out at room temperature with an incidence angle of 1° and with the polarization vector parallel to the sample surface ($E \perp c$). For each sample the integration time for each energy point and the number of acquired spectra are chosen in order to collect $\approx 10^6$ counts on the final averaged spectrum. Bragg diffraction peaks are eliminated by selecting the elements of the fluorescence detector or by manually de-glitching the affected spectra. In addition, before and after each measurement a metallic Mn reference foil is measured in transmission mode to check the stability of the energy scale and to provide an accurate calibration. Considering the present optics setup an energy resolution of ≈ 0.2 eV is obtained at 6539 eV.

In our context, the EXAFS signal $\chi(k)$ is extracted from the absorption raw data, $\mu(E)$, with the VIPER program³⁶ employing a smoothing spline algorithm and choosing the energy edge value (E_0) at the half height of the energy step (Sec. V C). The quantitative analysis is carried out with the IFEFFIT/ARTEMIS programs^{37,38} in the frame of the atomic model described below. Theoretical EXAFS signals are computed with the FEFF8 code³⁹ using muffin tin potentials and the Hedin-Lunqvist approximation for their energy-dependent part. In order to reduce the correlations between variables, the minimum set of free fitting parameters used in the analysis is: ΔE_0 (correction to the energy edge), S_0^2 (amplitude reduction factor), ΔR_0 , ΔR_1 (lattice expansion factors, respectively, for the first Mn-N coordination shell distances and all other upper distances) and σ_i^2 Debye-Waller factor for the i^{th} coordination shell around the absorber plus a correlated Debye model⁴⁰ for multiple scattering paths with a fitted Debye temperature of 470(50) K.⁴¹

D. SQUID experimental

The magnetic properties have been investigated in a Quantum Design MPMS XL 5 SQUID magnetometer between 1.85 and 400 K and up to 5 T. For magnetic studies the samples are typically cut into (5×5) mm² pieces, and both in- and out-of-plane orientations are probed. The (Ga,Mn)N layers are grown on 330 μm thick sapphire substrates, so that the TM-doped overlayers constitute only a tiny fraction of the volume investigated, and due to the substantial magnetic dilution their magnetic moment is very small to small when compared to the diamagnetic signal of the substrate. Therefore, a simple subtraction of a diamagnetic component originating from the sapphire substrate and linear with the field only exposes the resulting data to various artifacts related to the SQUID system and to arrangement of the measurements, as already discussed in Refs. 28, 42, and 43. In order to circumvent this issue, the magnetic data presented in this paper are obtained after subtracting the magnetic response of a sapphire substrate with dimensions equivalent to those of the investigated sample, independently measured on the same holders and according to the same experimental procedure. This method, in particular, eliminates a spu-

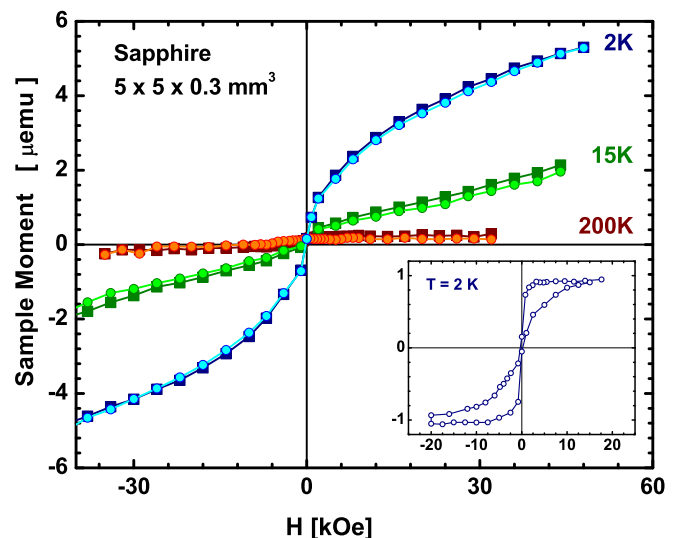


FIG. 1: (Color online) Magnetic response at 2, 15, and 200 K of a typical $(5 \times 5 \times 0.3)$ mm³ sapphire substrate measured for both in-plane (darker shade squares) and out-of-plane (lighter shade circles) configurations after the application of a correction linear in the magnetic field and proportional to the magnetic susceptibility of sapphire at 200 K. The magnetic moment obtained in this way at 2 K reaches a value that would give a magnetization of ~ 1 emu/cm³ for (a typical) 200 nm thick layer. Inset: $m(H)$ at 2 K for the same sapphire sample, but without correction. The axes labels are the same as in the main panel. This ferromagnetic-like signal is isotropic, decreases with temperature and vanishes above 15 K.

rious magnetic contribution that is due to the sapphire substrate and is not-linear with the field and, moreover, depends on the temperature. As exemplified in Fig. 1 this extra $m(T, H)$ constitutes a nontrivial and quite sizable contribution to the signal of interest. Additionally - as shown in the inset to this figure - the sapphire itself may convey a ferromagnetic response to the signal at the lowest temperatures. We have also made sure that this method is adequate to eliminate another weak and ferromagnetic-like contribution appearing in the data after subtracting only the compensation linear in the field. This fault is caused by an inaccuracy in the value of the magnetic field as reported by the SQUID system, which assumes that the field acting on the sample is strictly proportional to the current sent to the superconducting coil, and disregards the magnet remanence due to the flux pinning inside the superconducting windings.⁴⁴ This remanence in our 5 T system is as high as -15 Oe after the field has been risen to $H > +1$ T and results in a zero field magnetic moment of $+2 \times 10^{-7}$ emu for our typical sapphire substrate. Although the value is small, it linearly scales with the mass of the substrate and it exceeds the magnitude of the signal expected from a submicrometer thin layer of a DMS film.

E. SIMS experimental

The overall Mn concentration in the epilayers has been evaluated via secondary-ion mass spectroscopy (SIMS). The SIMS analysis is performed by employing Caesium ions as the primary beam with the energy set to 5.5 keV and the beam current kept at 150 nA. The raster size is $150 \times 150 \mu\text{m}^2$ and the secondary ions are collected from a central region of $60 \mu\text{m}$ in a diameter. The Mn concentration is derived from MnCs+ species, and the matrix signal NCs+ was taken as reference. Mn implanted GaN is used as a calibration standard.

IV. STRUCTURAL PROPERTIES

As already underlined, it is necessary to ascertain if the investigated material contains any secondary phases, nanoclusters or precipitates. In this context, it has been realized recently^{18,21,28,45} that the limited solubility of transition metals in semiconductors can lead to a chemical decomposition of the alloy, *i.e.* the formation of regions with the same crystal structure of the semiconductor host, but with respectively high and low concentration of magnetic constituents. In this work the structural properties of the system are analyzed by SXRD, HRTEM and EXAFS.

A. HRXRD and SXRD - results

In order to verify the homogeneity of the grown (Ga,Mn)N layers, conventional XRD measurements have been routinely performed. From rocking curves around the GaN (002) diffraction peak, the crystal quality from the FWHM is verified and we obtain values in the range 240 to 290 arcsec, indicating a high degree of crystal perfection of the layers. For the (Ga,Mn)N (002) diffraction peak we observe a shift to lower angles with increasing Mn concentration in the acquired $\omega/2\theta$ scans. This shift points to an increment in the c -lattice constant, as it has been also reported by others.^{46,47} Apart from the diffraction peak shift, no evidence for second phases is observed in the XRD measurements. These results have been confirmed by the SXRD diffraction spectra reported in Fig. 2(a), where no crystallographic phase separation is detected over a broad range of Mn concentrations.

The lattice parameters are determined by averaging the values for the two symmetric SXRD diffractions (004) and (006) for the c -parameter, and one asymmetric diffraction (104) for the a -parameter. The variation of the lattice parameters with increasing incorporation of Mn is presented in Fig. 2b.

To obtain further information on the solubility of Mn in our (Ga,Mn)N layers, *in situ* annealing experiments have been carried out at the ESRF BM20 beamline. Sample 400A was annealed up to 900°C in N-rich atmosphere at a pressure of 200 mbar, to compensate the nitrogen

loss during annealing. Several radial scans have been acquired upon increasing the sample temperature in subsequent 100°C steps, and realignment was performed after reaching each temperature. The diffraction curves upon annealing are shown in Fig. 3, and no additional diffraction peaks related to the formation of secondary phases have been detected over the whole process. This leads us to conclude that the considered (Ga,Mn)N grown with Mn concentration below the solubility limit at the given deposition conditions is stable in the dilute phase upon annealing over a considerable thermal range. This behavior is to be contrasted with the one reported for dilute (Ga,Mn)As, where annealing at elevated temperatures provokes the formation of either hexagonal or zinc-blende MnAs nanocrystals.^{48,49}

B. HRTEM results

HRTEM has been carried out on all (Ga,Mn)N layers under consideration and independently of the Mn concentration no evidence of crystallographic phase separation could be found. This is also confirmed by selected

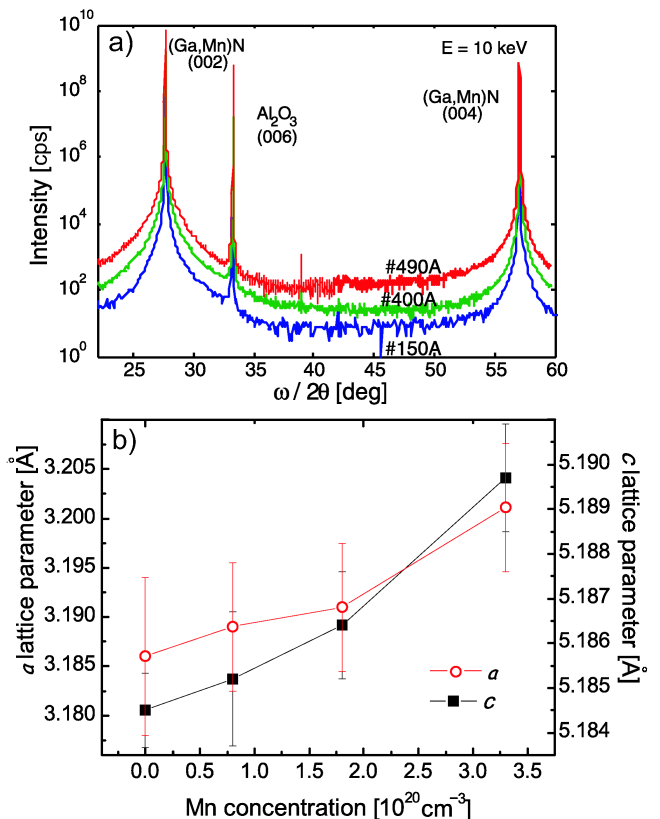


FIG. 2: (Color online) a) SXRD spectra for (Ga,Mn)N samples showing no presence of secondary phases over a broad range of concentration of the magnetic ions. b) Lattice parameters *vs.* Mn concentration. Values for an undoped GaN layer are added for reference

area electron diffraction (SAED) patterns (not shown) recorded on different areas of each sample, where no satellite diffraction spot apart from wurtzite GaN are detected. In Fig. 4, an example of the HRTEM images acquired along the $[10\bar{1}0]$ (a) and $[11\bar{2}0]$ (b) zone axis, respectively is given. Through measurements previously reported and carried out with the same microscope, we have been able to discriminate in (Ga,Fe)N different phases of Fe-rich nanocrystals as small as 3 nm in diameter, and also to detect mass contrast indicating the local aggregation of Fe-ions.^{18,50} The HRTEM images in Fig. 4, in contrast to the case of phase separated (Ga,Fe)N, strongly suggest that the (Ga,Mn)N film here studied are in the dilute state

The EDS spectra collected on the (Ga,Mn)N layers provide significant signatures of the presence of Mn, as evidenced in Fig. 5. The EDS detector and the software we used here identify the Mn elements automatically, and are sensitive to Mn concentrations as low as 0.1% (atomic%). The Mn concentration for sample 300A and reported in Fig. 5 is found to be 0.18% (atomic%).

C. EXAFS results

EXAFS (Ref. 51) is a well established tool in the study of semiconductor heterostructures and nanostructures⁵² and has proven its power as a chemically sensitive local probe for the site identification and valence state of Mn and Fe dopants in GaN DMS.^{53–57} The crystallinity of the films and the optimal signal to noise ratio of the collected spectra are demonstrated by the large number of atomic shells visible and reproducible by the fits below 8 Å in the Fourier-transformed spectra reported in Fig. 6 for the two representative samples 100A and 490A, re-

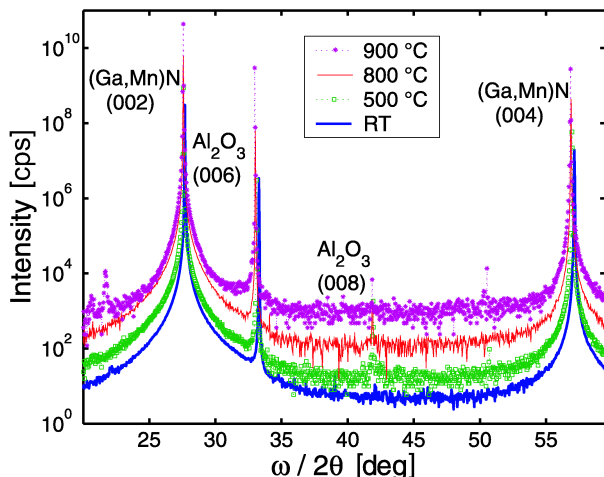


FIG. 3: (Color online) *In situ* XRD spectra upon annealing of sample 400A at different temperatures: no formation of secondary phases is detected up to an annealing temperature of 900 °C.

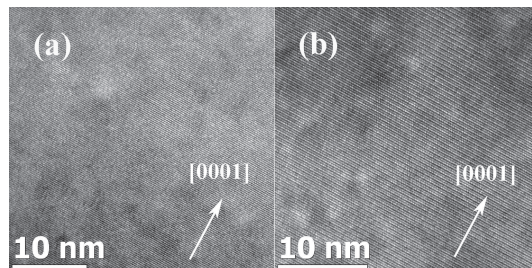


FIG. 4: HRTEM images: along $[10\bar{1}0]$ (a) and along the $[11\bar{2}0]$ zone axis (b).

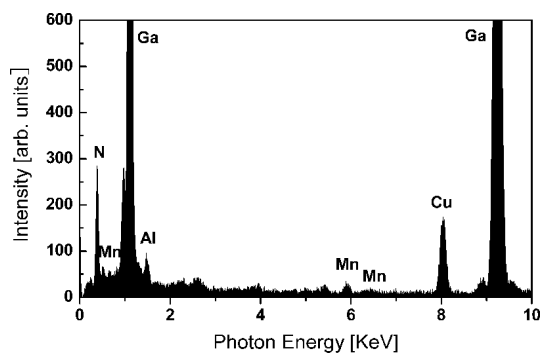


FIG. 5: EDS spectrum of sample 300A, with the identification of the Mn peaks [L_{α} (0.636 keV), K_{α} (5.895 keV) and K_{β} (6.492 keV)].

spectively. In addition, the homogeneous Mn incorporation along the layer thickness is tested by measuring the Mn fluorescence yield (at a fixed energy of 6700 eV) as a function of the incidence angle (not shown). The EXAFS response of these two samples is qualitatively equivalent, as evidenced in Fig. 6, and this is confirmed by the quantitative analysis. The best fits are obtained by employing a substitutional model of one Mn at a Ga site (Mn_{Ga}) in a wurtzite GaN crystal (using the lattice parameters previously found by SXRD). The possible presence of additional phases in the sample as octahedral or tetrahedral interstitials (Mn_I^O , Mn_I^T) in GaN or Mn_3GaN clusters⁵⁸ has been checked by carrying out fits with a two phases model. The fraction of the Mn_{Ga} is found to be 98(4) % for the pair Mn_{Ga} - Mn_3GaN , 99(3)% for the pair Mn_{Ga} - Mn_I^O and 97(3)% for the pair Mn_{Ga} - Mn_I^T , respectively. With these results we can safely rule out the occurrence of phases other than Mn_{Ga} , at least above 5% level.

The local structure parameters found for the measured samples are equivalent within the error bars (reported on the last digit within parentheses) and averaged values are given for simplicity. The value of the amplitude reduction factor $S_0^2 = 0.95(5)$ demonstrates the good agreement with the theoretical coordination numbers for Mn_{Ga} (considering the in-plane polarization) and the correction to the energy edge $\Delta E_0 = -7(1)$ eV supports the XANES analysis (Sec. V C). With respect to the lattice parameters previously found by SXRD,

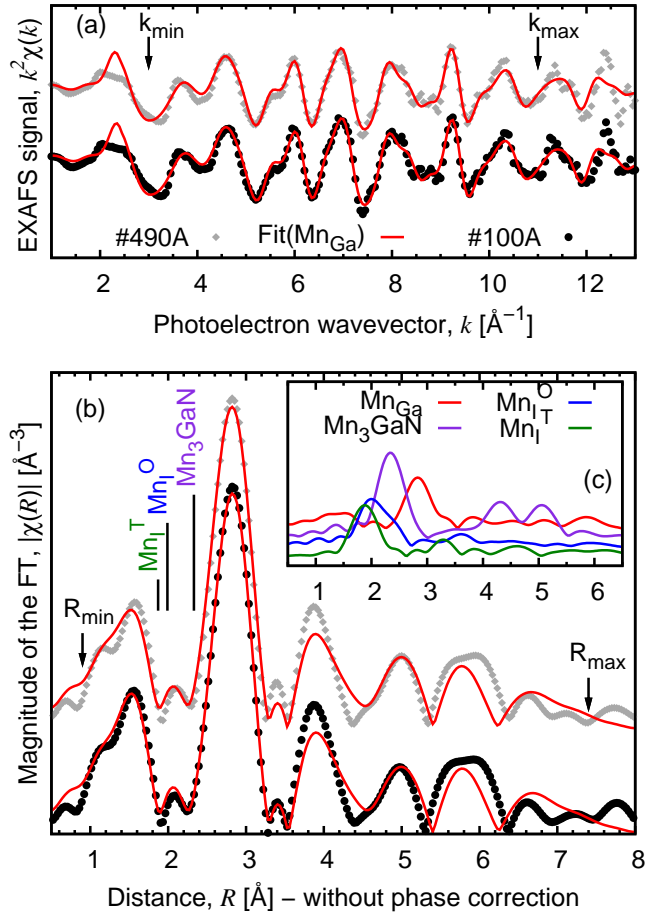


FIG. 6: (Color online) k^2 -weighted EXAFS signal, (a), for samples 100A (circles) and 490A (diamonds) with relative best fits (solid line) in the region $[R_{\min}-R_{\max}]$ and, (b), amplitude of the Fourier transforms (FT) carried out in the range $[k_{\min}-k_{\max}]$ by an Hanning window (slope parameter $dk=1$); the vertical lines indicate the position of the main peaks in the FT of the Mn_I^T , Mn_I^O and Mn_3GaN additional structures. Their possible presence would be promptly detected as they fall in a region free from other peaks. FEF8 simulations, (c), for the tested theoretical models as described in the text.

the long range distortion fits within the error ($\Delta R_1 = 0.1(2) \%$), while the Mn-N nearest neighbors have a $\Delta R_0 = 2.5(5) \%$ (expansion to $1.99(1) \text{ \AA}$), in line with previously reported experimental results⁵⁴⁻⁵⁶ and recent *ab initio* calculations.⁵⁹ Finally, all the evaluated σ_i^2 attest around the average value of $8(2) \cdot 10^{-3} \text{ \AA}^{-2}$, confirming the high crystallinity of the layers.

V. PROPERTIES OF HOMOGENEOUS SINGLE-PHASE (Ga,Mn)N

Thus, SXRD, HRTEM and XAFS experiments have confirmed the wurtzite structure of the samples, the absence of secondary phases, and the location of Mn in the Ga sublattice of the wurtzite GaN crystal. Further-

more, the samples have been investigated to determine the actual Mn concentration and the charge state of the magnetic ions.

A. Determination of the Mn concentration

The depth profiling capabilities of SIMS provide not only an accurate analysis of the (Ga,Mn)N layers composition, but allow also to monitor the changes in composition along the sample depth. The SIMS depth profiles reported in Figs. 7(a) and (b) give evidence that the distribution of the Mn concentration n_{Mn} in the investigated films is essentially uniform over the doped layers, independent of the magnetic ions content as well as that the interface between the (Ga,Mn)N overlayer and the GaN buffer layer is sharp. This is confirmed by EDS studies, which with the sensitivity around 0.1% at. do not provide any evidence for Mn diffusion into the buffer. The determined total Mn concentration increases with increasing $MeCp_2Mn$ flow rate and the corresponding n_{Mn} values for the considered samples can be found in Table I.

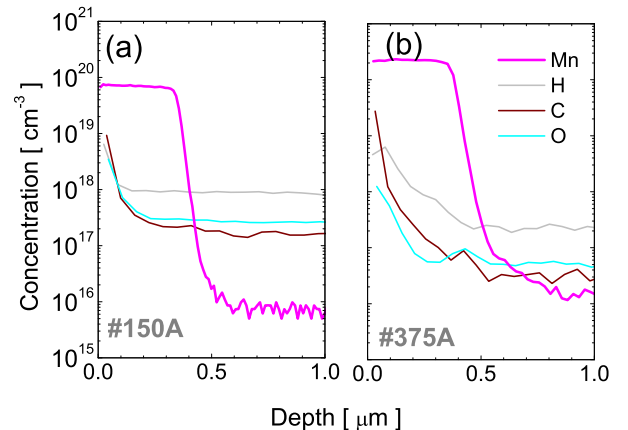


FIG. 7: (Color online) SIMS depth profiles of Mn, C, O and H for the samples: a) 150A and b) 375A.

B. Energy levels introduced by Mn impurities

The character of the paramagnetic response of DMS depends crucially on the magnetic ion configuration. In III-V semiconductors, Mn in the impurity limit substitutes the cation site giving three electrons to the crystal bond. Depending on the compensation ratio, Mn can exist in three different charge states and electron configurations, namely: i) ionized acceptor Mn^{2+} , with five electrons localized in the Mn d shell. The electronic configuration of Mn^{2+} is d^5 , and the ground level of the ion at zero magnetic field is a degenerate multiplet with vanishing orbital momentum ($L = 0$, $S = 5/2$). The magnetic moment of the ion results solely from the spin,

and its magnetic contribution can be described by a standard Brillouin function for any orientation of the magnetic field. The neutral configuration of Mn^{3+} ($S = 2$, $L = 2$) can be realized in two ways: ii) by substitutional manganese d^4 with four electrons tightly bound in the Mn d shell; iii) Mn^{2+} + hole (d^5 + hole) with five electrons in the Mn d shell and a bound hole localized on neighboring anions.

C. XANES results

The XANES spectra allow to determine the redox-state of the probed species and give information on the structure of the surroundings of the absorbing atom.⁶⁰ Basically, the near edge region resembles the density of those empty states, that are accessible via optical transitions from the Mn $1s$ shell.

The goal of our XANES analysis is to determine the valence state of Mn and to confirm the Mn_{Ga} incorporation, in comparison to the findings and analysis carried out previously for molecular beam epitaxy (MBE)-grown (Ga,Mn)N, and interpreted in terms of Mn^{3+} (Refs. 11 and 61) or Mn^{2+} (Ref. 62). In order to assign the Mn valence state, first of all we proceed with a comparison of the position of the absorption Mn K-edge to reference compounds, like Mn-based oxides since we do not have available data on Mn-nitrides. This procedure was already adopted by other groups^{55,62} but its reliability could be questionable; to clarify this point *ab initio* calculations are also performed.

As shown in Fig. 8, the XANES spectra determined for two samples differing in Mn concentrations (100A and 490A) are identical, confirming a conclusion from the SQUID data on the independence of the Mn charge state of the Mn concentration. In Fig. 8(a) three spectra collected in transmission mode from commercial powders of MnO, Mn_2O_3 and MnO_2 , with Mn-valence states 2+, 3+, 4+, respectively, are used as reference. As seen, with the increasing charge state, the edge moves to a higher energy, as the accumulated positive charge shifts downwards in energy more the $1s$ Mn shell than the valence states, in agreement with the Haldane-Anderson rule.

Usually, the edge position is taken at the first inflection point of the plot, but in the present case (since the oxide spectra exhibit a broad peak that modifies the slope at the edge) a better estimate of the edge position is obtained by considering the energy of the half step-height of the background function. In both investigated samples this lies at 6550.0(5) eV. For the oxides, their half-height energies are determined to be 6545.7(5) eV, 6550.3(5) eV, 6553.3(5) eV for MnO, Mn_2O_3 and MnO_2 , respectively. This would strongly suggest that we deal with Mn^{3+} , in line with the SQUID results (Sec. VI A). On the other hand, taking the position of the inflection points, the determined charge state would be 2+, as reported in Ref. 62. This demonstrates that, in this case, relying only on the edge position to determine the valence state

is prone to error and strongly depends on the local surrounding of the probed species.⁶³

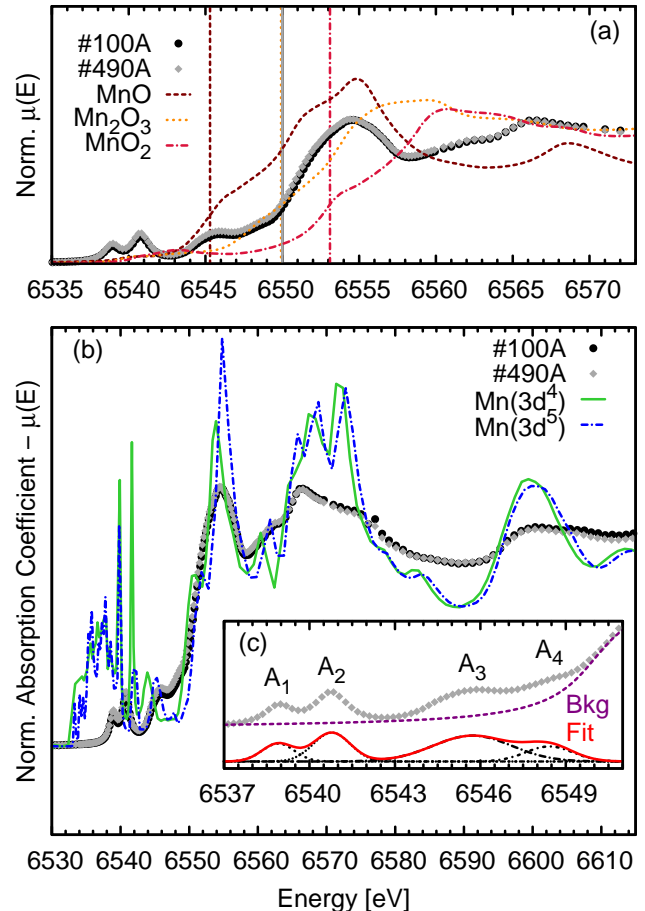


FIG. 8: (Color online) Normalized XANES spectra of the samples 100A and 490A (points) compared with: (a) the reference manganese oxides (MnO , Mn_2O_3 , MnO_2) - the chosen edge positions are highlighted by vertical lines; (b) *ab initio* absorption spectra (without convolution) for Mn_{Ga} in the $3d^4$ and $3d^5$ electronic configurations. The inset (c) shows the method used to extract the results of Table II, focusing the near-edge region for sample 490A with the baseline (Bkg), the relative fit and its components (A_1 - A_4).

To clarify this point, we look at the pre-edge peaks of the XANES lines (Fig. 8(b),(c)). In both probed samples, there are two defined peaks below the absorption edge, which we label A_1 and A_2 , while the edge itself shows two shoulders, A_3 and A_4 . In Table II the results of Gaussian fits performed by using an arctan-function as baseline, are reported. Similar findings were previously interpreted^{61,64} as indicative of the Mn^{3+} charge state. The peaks A_1 and A_2 correspond to the transitions to Mn $3d$ - $4p$ hybrid states, while A_3 and A_4 end in the GaN higher conduction bands at positions with a high density of $4p$ states. Due to the tetrahedral environment, the Mn $3d$ -levels split in two nearly degenerate e - and three nearly degenerate t_2 -levels for each spin-direction. The actual position of those states with respect to the

TABLE II: Position P , integrated intensity I and full width at half maximum W of the Gaussians fitted to the peaks before and at the absorption edge. The background function is used to normalize the spectra.

	100Å			490Å		
	P (eV)	I	W (eV)	P (eV)	I	W (eV)
	± 0.2	± 0.05	± 0.1	± 0.2	± 0.05	± 0.1
A ₁	6538.9	0.18	1.5	6538.9	0.18	1.3
A ₂	6540.8	0.32	1.6	6540.8	0.33	1.5
A ₃	6545.8	0.70	3.6	6545.7	0.64	3.3
A ₄	6548.7	0.28	2.1	6548.4	0.22	2.0

GaN band structure is still a matter of debate, but from absorption^{65,66} and photoluminescence⁶⁷ measurements it is known that for the majority spin carriers in Mn³⁺, the e -levels lie around 1.4 eV below the t_2 -levels of Mn incorporated substitutionally in GaN, and the t_2 -level, *i.e.*, the Mn³⁺/Mn²⁺ state is located about 1.8 eV above the valence band. An interpretation of simulations applied to x-ray absorption spectra is given in Refs. 61 and 68, and states that, due to crystal field effects, the $3d$ - and $4p$ -states can hybridize, making transitions from the $1s$ -level to the t_2 -levels dipole allowed, while the interaction of the e -levels with the $4p$ orbitals is much weaker and cannot be seen in K-edge XANES.

In view of the above discussion we explain the physical mechanism beyond the observed data considering possible *final* states of the transitions from the $1s$ Mn shell. The final state corresponding to the A₁ peak is Mn²⁺, *i.e.* a ⁶A₁ state (⁶S for the spherical symmetry), consisting of $e^{2\uparrow}$ and $t_2^{3\uparrow}$ one electron levels. The A₂ peak can be interpreted as a crystal field multiplet derived from the ⁴G state consisting of $e^{2\uparrow}t_2^{2\uparrow}t_2^{\downarrow}$, and lying about 2.5 eV higher than the A₁ state. Apart from what reported in literature, a reason why A₁ and A₂ are assigned to localized Mn-states is that from the previous EXAFS analysis (Sec. IV C) we obtain an absorption edge value of 6543(1) eV, between the energies of the A₂ and A₃ peaks, meaning that electrons excited to A₁ and A₂ can not backscatter at the surrounding atoms, and they are thus localized. This assignment gives a valuable information, namely, that there is an empty state in the majority-spin t_2 -level confirming that most of the incorporated Mn-ions are really in the 3+ valence state, in agreement with the conclusions of Refs. 11 and 61. The model explains also the presence of only one pre-edge peak in the case of (Ga,Mn)As and p -(Zn,Mn)Te.⁶¹ In those systems we deal with Mn²⁺ and delocalized holes, so that the final state of the relevant transitions corresponds to the Mn d^6 level, involving only one spin orientation. On the other hand, the XANES data do not provide information on the radius of the hole localization in (Ga,Mn)N, in other words, whether the Mn³⁺ configuration corresponds to the d^4 or rather to the $d^5 + h$ situation, where the relevant t_2 hole state is partly built from the neighboring

anion wave functions owing to a strong $p - d$ hybridization.

We also have simulated the Mn_{Ga} K-edge absorption spectra in a Ga₉₅Mn₁N₉₆ cluster (a $4a \times 4a \times 3c$ supercell, corresponding to 1% Mn concentration) focusing the attention on the Mn electronic configuration: $3d^4$ and $3d^5$. The calculation is conducted within the multiple-scattering approach implemented in FDMNES⁶⁹ using muffin-tin potentials, the Hedin-Lunqvist approximation for their energy-dependent part, a self-consistent potential calculation⁷⁰ for enhancing the accuracy in the determination of the Fermi energy and the in-plane polarization ($E \perp c$). Despite it is common practice to report convoluted spectra to mimic the experimental resolution, we find out that this procedure can arbitrary change the layout of the pre-edge peaks and for this reason it is preferred to show non-convoluted data [Fig. 8(b)]. Regarding the fine structure of the simulated spectra, we have a good agreement with experimental data, confirming the Mn_{Ga} incorporation as found by the EXAFS analysis (Sec. IV C). On the other hand, the simulated pre-edge features need a further investigation: the experimental intensity of A₁ and A₂ and the position of A₃ are not properly reproduced. This could be due to some neglected effects in the employed formalism, as explained in Ref. 61, where the two peak structure was reproduced theoretically within a more elaborated model.

VI. MAGNETIC PROPERTIES

A. SQUID results

We investigate both the temperature dependence of the magnetization M at a constant field $M(T)$ and the sample response to the variation of the external field at a constant temperature $M(H)$. The same experimental routine is repeated for both in-plane and out-of-plane configurations, that is with magnetic field applied perpendicular and parallel to the hexagonal c -axis, respectively. In Fig. 9 representative low temperature $M(H)$ data for both orientations are reported. We note that these curves exhibit a paramagnetic behavior with a pronounced anisotropy with respect to the c -axis of the crystal. This indicates a nonspherical Mn ion configuration, expected for a $L \neq 0$ state. At the same time we report an absence of any ferromagnetic-like features, that—on the other hand—are typical for (Ga,Fe)N layers²⁸ at these concentrations of the magnetic ions, supporting the absence of crystallographic phase separation in our layers, as suggested by the SXRD and HRTEM studies. The same finding additionally indicates that both chemical phase separation (spinodal decomposition) and medium-to-long range ferromagnetic spin-spin coupling are also absent in this dilute layers. The latter allows us to treat the Mn ions as completely non-interacting, at least in the first approximation. The solid lines in Figs. 9 and 10 represent fits to our experimental data on the param-

agnetic response of non-interacting Mn^{3+} ions ($L = 2$, $S = 2$) with the trigonal crystal field of the wurtzite GaN structure and the Jahn-Teller distortion taken into account (details in Sec. VIB). The overall match validates our approach, which, in turn, is consistent with previous findings^{71,72} that without an intentional codoping, or when the stoichiometry of GaN:Mn is maintained, Mn is occupying only the neutral Mn^{3+} acceptor state. Interestingly, all theoretical lines in Figs. 9 and 10 are calculated employing only one set of crystal field parameters (as listed in Table III) having the Mn^{3+} concentration $n_{\text{Mn}^{3+}}$ as the only adjustable parameter for each individual layer. In Fig. 11 the $n_{\text{Mn}^{3+}}$ values as a function of the manganese precursor flow rate are given together with the total Mn content x_{Mn} as determined by SIMS.

However, there are hints that the interaction between Mn spins may play a role for $x \gtrsim 0.6\%$. In Fig. 12 the $M(H)$ normalized at high field ($H = 50$ kOe) to their in-plane values, are reported. The fact that the shape of their magnetization curves is independent of x for $x \lesssim 0.6\%$ means that the interactions between Mn ions are unimportant for these dilutions. On the other hand, the $M(H)$ for a layer with $x = 0.9\%$ (490A) secedes markedly from the curves for samples with $x \lesssim 0.6\%$, indicating that supposedly ferromagnetic Mn-Mn coupling starts to emerge with increasing relative number of Mn nearest neighbors in the layers. Nevertheless, due to the generally low Mn concentration in the considered samples, no conclusive statement about the strength of the magnetic couplings can be drawn from our magnetization

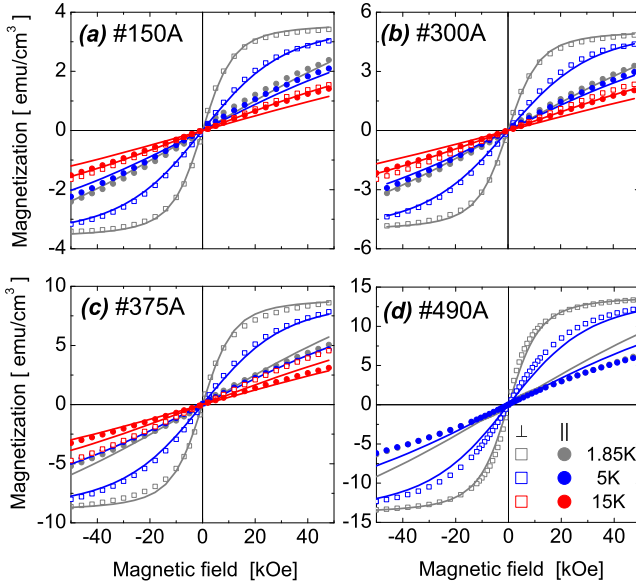


FIG. 9: (Color online) Magnetization measurements at 1.85, 5, and 15 K of $\text{Ga}_{1-x}\text{Mn}_x\text{N}$ as a function of the magnetic field applied parallel (closed circles) and perpendicular (open squares) to the GaN wurtzite c -axis. The solid lines show the magnetization curves calculated according to the group theoretical model for non-interacting Mn^{3+} ions in wz-GaN.

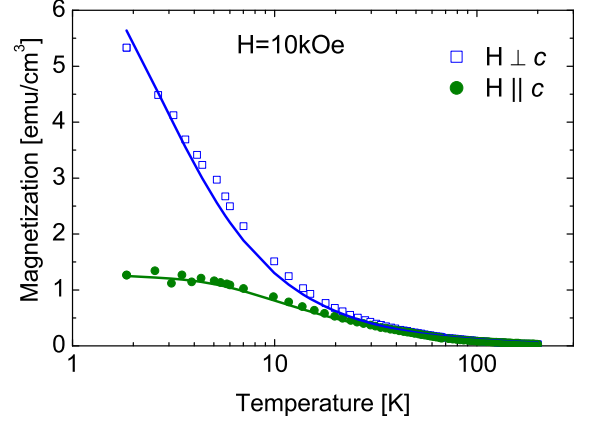


FIG. 10: (Color online) Temperature dependence of the magnetization M for sample 375A (points) at $H = 10$ kOe. The solid lines represent the magnetization calculated within the group theoretical model of non-interacting Mn^{3+} ions in wz-GaN.

data. Interestingly, depending on the very nature of the Mn centers both ferromagnetic and/or antiferromagnetic $d-d$ interactions can emerge in (Ga,Mn)N. The presence of Mn^{2+} ions essentially leads to antiferromagnetic superexchange, as in II-Mn-VI DMS, where independently of the electrical doping, the position of the Mn d -band guarantees its $3d^5$ configuration. Significantly, the same antiferromagnetic $d-d$ ordering and paramagnetic behavior typical for $S = 5/2$ of Mn^{2+} was reported in n -type bulk (Ga,Mn)N samples containing as much as 9% of Mn.⁷³ On the other hand, calculations for Mn^{3+} within the DFT point to ferromagnetic coupling^{74,75} and, experimentally, a Curie temperature $T_C \simeq 8$ K was observed in single-phase $\text{Ga}_{1-x}\text{Mn}_x\text{N}$ with $x \simeq 6\%$ and the majority of Mn atoms in the Mn^{3+} charge state.^{11,76} Our experimental data seems to support these findings and to extend their validity towards the very diluted limit. Finally, we remark that the carrier-mediated ferromagnetism can be excluded at this stage due to the insulating character of the samples, confirmed by room temperature four probe resistance measurements and consistent with the mid-gap location of the Mn acceptor level.

The observations presented here point to an uniqueness of Mn in GaN. The fact that $\text{Ga}_{1-x}\text{Mn}_x\text{N}$ with $x \lesssim 1\%$ is paramagnetic without even nanometer-scale ordering should be contrasted with GaN doped with other TM ions. Depending on the growth conditions, the TM solubility limit is rather low and typically, except for Mn, it is difficult to introduce more than 1% of magnetic impurities into randomly distributed substitutional sites. For example, the solubility limit of Fe in GaN has been shown to be $x \approx 0.4\%$ at optimized growth conditions (see Ref. 28), but signatures of a nanoscale ferromagnetic coupling are observed basically for any dilution.²⁸ The relatively large solubility limit of Mn in GaN, in turn, has a remarkable significance in the search for long-range coupling mediated by itinerant carriers.^{1,6} Not only it

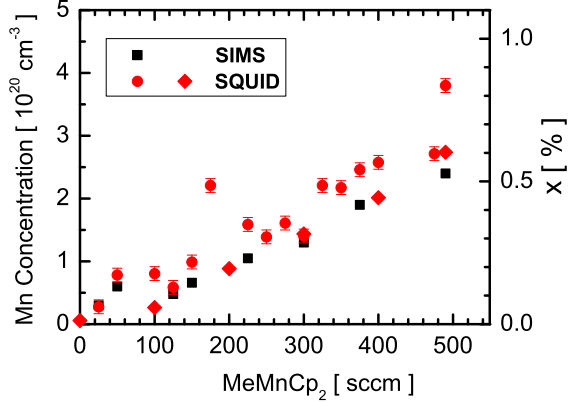


FIG. 11: (Color online) Mn concentration n_{Mn} obtained from magnetization measurements (circles - series A, diamonds - series B) and SIMS (squares - series A) as a function of the Mn precursor flow rate.

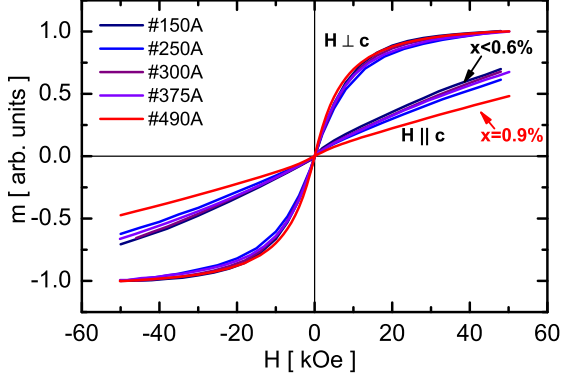


FIG. 12: (Color online) Magnetization curves at $T=1.85\text{K}$ of five $\text{Ga}_{1-x}\text{Mn}_x\text{N}$ samples normalized with respect to their in plane magnetization at $H = 50 \text{ kOe}$.

lets foresee a high concentration of substitutional Mn—important for the long-range ordering—but it can ensure that the effects brought about by carriers are not masked by signals from nanocrystals with different phases.

B. Magnetism of Mn^{3+} ions - theory

The Mn concentration in our samples is then $x \lesssim 1\%$ as evaluated by means of various characterization techniques (subsection V A), implying that most of the Mn ions ($\geq 90\%$) have no nearest magnetic neighbors. Therefore, the model that considers the Mn ions as single, non-interacting magnetic centers should provide a reasonable picture. To describe the Mn^{3+} ion we follow the group theoretical model developed for Cr^{2+} ion by Vallin^{77,78} and then successfully used for a Mn-doped hexagonal GaN semiconductor.^{79,80} It should be pointed out that symmetry considerations cannot discriminate between the d^5 +hole and d^4 many-electron configurations of the Mn ions, therefore the presented model should be ap-

plicable to both configurations. Through this section, the capital letters T_i ($i = 1, 2$), E denote the irreducible representations of the point group for the multielectron configurations in contrast to the single electron states indicated by the small letters d , e , t_2 .

We consider a Mn ion that in its free state is in the electronic configuration d^5s^2 of the outer shells. When substituting for the group III (s^2p) cation site, Mn gives three of its electrons to the crystal bond and assumes the Mn^{3+} configuration. In a tetrahedral crystal field, the relevant levels are five-fold degenerate with respect to the projection of the orbital momentum and are split by this field and by hybridization with the host orbitals into two sublevels e and t_2 with different energies. In the tetrahedral case the e states lie lower than the t_2 states. This fact can be understood by analyzing the electron density distribution of the t_2^{xy} , t_2^{yz} , t_2^{zx} and $e^{x^2-y^2}$, e^{z^2} levels. The density of the t_2 state extends along the direction toward the N ligand anions, while the e orbital has a larger amplitude in the direction maximizing the distance to the N ion and due to the negative charge of the N anions, the t_2 energy increases. However, the relevant, *i.e.*, the uppermost t_2 state may actually originate from orbitals of neighboring anions, pull out from the valence band by the p - d hybridization.⁸¹ If the system has several localized electrons, they successfully occupy the levels from the bottom, according to Hund's first rule, and keep their spins parallel. By considering the full orbital and spin moments, the Mn^{3+} center can be described through the following set of quantum numbers (Lm_LSm_S) with $L = 2$ and $S = 2$. However, we underline that this procedure can be used only if the intra-atomic exchange Δ_{ex} interaction is larger than the splitting between the e and t_2 states $\Delta_{CF} = E_{t_2} - E_e$ ($\Delta_{ex} > \Delta_{CF}$). After this, the effect of the host crystal is taken into account as a perturbation like in the single electron problem. One forms first $2L + 1$ wave functions for the n -electron system determined by the Hund's rule, calculates the matrix elements for these states and determines the energy level structure. In this way, the impurity ions states are found and classified according to the irreducible representations of the crystal point group and characterized by the set ($\Gamma M_S m_S$) of quantum numbers, with M the number of the line of an irreducible representation $\Gamma = A_1, A_2, E, T_1, T_2$ of the corresponding point group. In the case of a Mn^{3+} ($L = 2, S = 2$) ion in a tetrahedral environment the ground state corresponds to the ${}^5T_2(e^2t_2^3)$ configuration with two electrons in the e and two electrons in the t_2 level. The ground state is three-fold degenerate, since there are three possibilities to choose two orbitals from three t_2 orbitals. The first excited state for the Mn^{3+} ion is ${}^5E(e^1t_2^3)$ (see Ref. 82).

The energy structure of a single ion in Mn^{3+} charge state can be described by the Hamiltonian

$$H = H_{CF} + H_{JT} + H_{TR} + H_{SO} + H_B, \quad (1)$$

where $H_{CF} = -2/3B_4(\hat{O}_4^0 - 20\sqrt{2}\hat{O}_4^3)$ gives the effect of

TABLE III: Parameters of the group theoretical model used to calculate the magnetization of $\text{Ga}_{1-x}\text{Mn}_x\text{N}$. All values are in meV.

B_4	B_2^0	B_4^0	\tilde{B}_2^0	\tilde{B}_4^0	λ_{TT}	λ_{TE}
11.44	4.2	-0.56	-5.1	-1.02	5.0	10.0

a host having tetrahedral T_d symmetry, $H_{JT} = \tilde{B}_2^0 \hat{\Theta}_4^0 + \tilde{B}_4^0 \hat{\Theta}_4^2$ is the static Jahn-Teller distortion of the tetragonal symmetry, $H_{TR} = B_2^0 \hat{O}_4^0 + B_4^0 \hat{O}_4^2$ represents the trigonal distortion along the GaN hexagonal c -axis, that lowers the symmetry to C_{3V} , $H_{SO} = \lambda \hat{L} \hat{S}$ corresponds to the spin-orbit interaction and $H_B = \mu_B (\hat{L} + 2\hat{S}) \mathbf{B}$ is the Zeeman term describing the effect of an external magnetic field. Here $\hat{\Theta}$, \hat{O} are Stevens equivalent operators for a tetragonal distortion along one of the cubic axes [100] and trigonal axis [111] $\parallel c$ (in a hexagonal lattice) and B_q^p , \tilde{B}_q^p , λ_{TT} , and λ_{TE} are parameters of the group theoretical model. As starting values we have used the parameters reported for Mn^{3+} in GaN:Mn,Mg ⁸⁰ which describe well the magneto-optical data on the intra-center absorption related to the neutral Mn acceptor in GaN. Remarkably, only a noticeable modification (about 10%) of λ_{TT} and B_2^0 has been necessary in order to reproduce our magnetic data (the remaining parameters are within 3% of their previously determined values.) Actually, the model with the parameter values collected in Table III describes both the magnetization $M(H)$ and its crystalline anisotropy (Figs. 9 and 10) as well as the position and the field-induced splitting of optical lines.⁸⁰

The ground state of the Mn^{3+} ion is an orbital and spin quintet 5D with $L = 2$ and $S = 2$. The term H_{CF} splits the 5D ground state into two terms of symmetry 5E and 5T_2 (ground term). The ${}^5E - {}^5T_2$ splitting is $\Delta_{CF} = 120B_4$. The nonspherical Mn^{3+} ion undergoes further Jahn-Teller distortion, that lowers the local symmetry and splits the ground term 5T_2 into an orbital singlet 5B and an higher located orbital doublet 5E . The trigonal field splits the 5E term into two orbital singlets and slightly decreases the energy of the 5B orbital singlet. The spin-orbital term yields further splitting of the spin orbitals. Finally, an external magnetic field lifts all of the remaining degeneracies.

For the crystal under consideration, there are three Jahn-Teller directions: [100], [010] and [001] (center A, B, C respectively).^{79,80} It should be pointed out that the magnetic anisotropy of the Mn^{3+} system originates from different distributions of nonequivalent Jahn-Teller centers in the two orientations of the magnetic field and the hexagonal axial field H_{TR} along the c -axis. This picture of Mn in GaN emphasizing the importance of the Jahn-Teller effect, which lowers the local symmetry and splits the ground term 5T_2 into an orbital singlet and a doublet, is in agreement with a recent *ab initio* study employing a hybrid exchange potential.⁵⁹

The energy level scheme of the Mn^{3+} ion is calculated

through a numerical diagonalization of the full 25×25 Hamiltonian (1) matrix. The average magnetic moment of the Mn ion $\mathbf{m} = \mathbf{L} + 2\mathbf{S}$ (in units of μ_B) can be obtained according to the formula:

$$\langle \mathbf{m} \rangle = Z^{-1} (Z_A \langle \mathbf{m} \rangle^A + Z_B \langle \mathbf{m} \rangle^B + Z_C \langle \mathbf{m} \rangle^C), \quad (2)$$

with Z_i ($i = A, B$ or C) being the partition function of the i -th center, $Z = Z_A + Z_B + Z_C$ and

$$\langle \mathbf{m} \rangle^i = \frac{\sum_{j=1}^N \langle \varphi_j | \hat{L} + 2\hat{S} | \varphi_j \rangle \exp(-E_j^i/k_B T)}{\sum_{j=1}^N \exp(-E_j^i/k_B T)}, \quad (3)$$

where E_j^i and φ_j are the j -th energy level and the eigenstate of the Mn^{3+} ion i -th center, respectively. As already mentioned, the Mn concentration in our samples is relatively small $x \lesssim 1\%$. Therefore, the model assuming a system of single Mn ions provides a reasonable description of the magnetic behavior. The macroscopic magnetization \mathbf{M} , shown in Figs. 9 and 10, can then be expressed in the form

$$\mathbf{M} = \mu_B \langle \mathbf{m} \rangle n_{Mn}, \quad (4)$$

where $n_{Mn} = N_{Mn}/V$ is the Mn concentration and N_{Mn} the total number of Mn ions in a volume V .

C. Search for hole-mediated ferromagnetism

As already mentioned, according to the theoretical predictions within the $p-d$ Zener model,^{1,6} RT ferromagnetism is expected in single-phase (Ga,Mn)N and related compounds, provided that a sufficiently high concentration of both substitutional magnetic impurities (near 5% or above) and valence-band holes will be realized. The latter condition is a more severe one, as the high binding energy of Mn acceptors in the strong coupling limit leads to hole localization.

Surprisingly, RT ferromagnetism in p -type $\text{Ga}_{1-x}\text{Mn}_x\text{N}$ with a Mn content as low as $x \approx 0.25\%$ was recently reported.¹³ The investigated modulation-doped structure consisted of a (Ga,Mn)N/(Al,Ga)N:Mg/GaN:Si (i - p - n) multilayer and a correlation between the ferromagnetism of the (Ga,Mn)N film at 300 K and the concentration of holes accumulated at the (Ga,Mn)N/(Al,Ga)N:Mg interface was shown. The interfacial hole density was controlled by an external gate voltage applied across the p - n junction of the structure, and a suppression of the FM features—already existing without the gate bias—took place for a moderate gate voltage applied. Apart from a high value of T_C , a puzzling aspect of the experimental results is the large magnitude of the spontaneous magnetization, $75 \mu\text{emu}/\text{cm}^2$.¹³ Since the

holes are expected to be accumulated in a region with a thickness of the order of 1 nm, the reported magnetic moment is about two orders of magnitude larger than the one expected for ferromagnetism originating from an interfacial region in (Ga,Mn)N with $x = 0.25\%$.

Nevertheless, we have decided to check the viability of this approach that not only seemed to result in high temperature FM in GaN:TM, but also allowed the all-electrical control of FM. Thus, we have combined the p -type doping procedures we previously optimized²⁷ with the growth of the dilute (Ga,Mn)N presented in this work to carefully reproduce the corresponding structure.¹³ The desired architecture of the investigated sample is confirmed by SIMS profiling (see Fig. 13) indicating the formation of well defined (Ga,Mn)N/(Al,Ga)N:Mg and (Al,Ga)N:Mg/GaN:Si interfaces. However, as shown in Fig. 14, no clear evidence of a ferromagnetic-like response is seen within our present experimental resolution of $\approx 0.3 \mu\text{emu}/\text{cm}^2$. To strengthen the point, we note here that the maximum error bar of our results ($\approx 0.7 \mu\text{emu}/\text{cm}^2$) corresponds to about 1/100 of the saturation magnetization reported in the assessed experiment. While the absence of a ferromagnetic response at the level of our sensitivity is to be expected, the presence of a large ferromagnetic signal found in Ref. 13 in a nominally identical structure is surprising. Without a careful structural characterization of the sample studied in Ref. 13 by methods similar to those we have employed in the case of our layers, the origin of differences in magnetic properties between the two structures remains unclear.

VII. SUMMARY

In this paper we have investigated $\text{Ga}_{1-x}\text{Mn}_x\text{N}$ films grown by MOVPE with manganese concentration $x \lesssim 1\%$. A set of experimental methods, including SXRD,

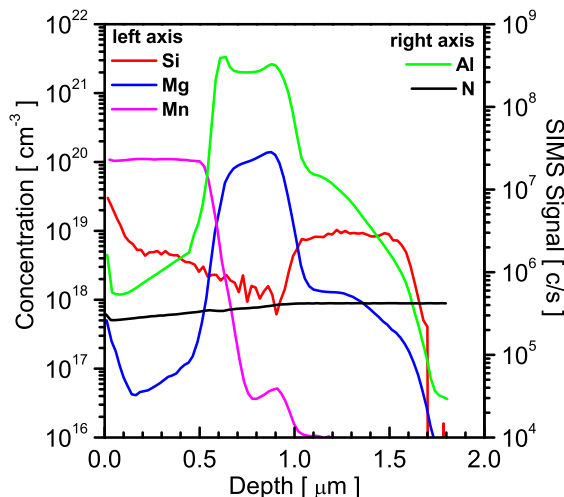


FIG. 13: (Color online) SIMS depth profiles of our (Ga,Mn)N/(Al,Ga)N:Mg/GaN:Si (i - p - n) structure.

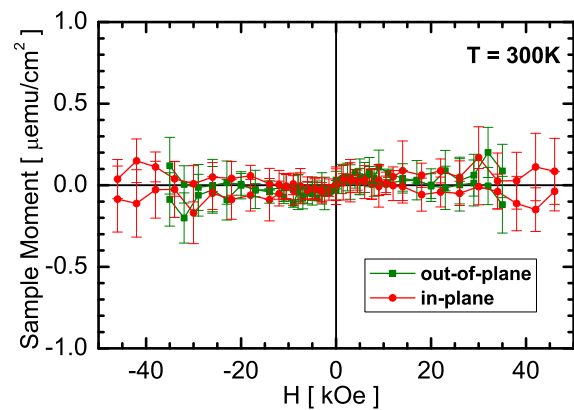


FIG. 14: (Color online) Room temperature magnetic signal from the (Ga,Mn)N/(Al,Ga)N:Mg/GaN:Si structure. For completeness, results of both in-plane and out-of-plane orientations are shown. Diamagnetic and paramagnetic contributions have been compensated.

HRTEM, and EXAFS, has been employed to determine the structural properties of the studied material. These measurements reveal the absence of crystallographic phase separation and a Ga-substitutional position of Mn in GaN. The findings demonstrate that the solubility of Mn in GaN is much greater than the one of Cr (Ref. 83) and Fe (Ref. 18) in GaN grown under the same conditions. Nevertheless, for the attained Mn concentrations and owing to the absence of band carriers, the Mn spins remain uncoupled. Accordingly, pertinent magnetic properties as a function of temperature, magnetic field and its orientation with respect to the c -axis of the wurtzite structure can be adequately described by the paramagnetic theory of an ensemble of non-interacting Mn ions in the relevant crystal field. Our SQUID and XANES results point to the $3+$ configuration of Mn in GaN. However, the collected information can not tell between d^4 and $d^5 + h$ models of the Mn^{3+} state, that is on the degree of hole localization on the Mn ions. A negligible contribution of Mn in the $2+$ charge state indicates a low concentration of residual donors in the investigated films. Our studies on modulation doped p -type $\text{Ga}_{1-x}\text{Mn}_x\text{N}/(\text{Ga},\text{Al})\text{N}:\text{Mg}$ heterostructures do not reproduce the high temperature robust ferromagnetism reported recently for this system.¹³

Acknowledgements

The work was supported by the FunDMS Advanced Grant of the European Research Council within the "Ideas" 7th Framework Programme of the EC, and by the Austrian Fonds zur Förderung der wissenschaftlichen Forschung (P18942, P20065 and N107-NAN). We also acknowledge H. Ohno and F. Matsukura for valuable discussions, G. Bauer and R.T. Lechner for their contribution to the XRD measurements as well as the support of

the staff at the Rossendorf Beamline (BM20) and at the Italian Collaborating Research Group at the European

Synchrotron Radiation Facility in Grenoble.

-
- * Electronic address: mikes@ifpan.edu.pl
† Electronic address: dietl@ifpan.edu.pl
‡ Electronic address: alberta.bonanni@jku.at
- ¹ T. Dietl, H. Ohno, F. Matsukura, J. Cibert, and D. Fer-
rand, *Science* **287**, 1019 (2000).
 - ² I. Žutić, J. Fabian, and S. Das Sarma, *Rev. Mod. Phys.*
76, 323 (2004).
 - ³ T. Jungwirth, J. Sinova, J. Mašek, J. Kučera, and A. H.
MacDonald, *Rev. Mod. Phys.* **78**, 809 (2006).
 - ⁴ K. Olejník, M. H. S. Owen, V. Novák, J. Mašek, A. C.
Irvine, J. Wunderlich, and T. Jungwirth, *Phys. Rev. B* **78**,
054403 (2008).
 - ⁵ M. Wang, R. P. Campion, A. W. Rushforth, K. W. Ed-
monds, C. T. Foxon, and B. L. Gallagher, *Appl. Phys.*
Lett. **93**, 132103 (2008).
 - ⁶ T. Dietl, H. Ohno, and F. Matsukura, *Phys. Rev. B* **63**,
195205 (2001).
 - ⁷ T. Dietl, *J. Phys.: Condens. Matter* **16**, S5471 (2004).
 - ⁸ M. L. Reed, N. A. El-Masry, H. H. Stadelmaier, M. K.
Ritums, M. J. Reed, C. A. Parker, J. C. Roberts, and
S. M. Bedair, *Appl. Phys. Lett.* **79**, 3473 (2001).
 - ⁹ J. I. Hwang, M. Kobayashi, G. S. Song, A. Fujimori,
A. Tanaka, Z. S. Yang, H. J. Lin, D. J. Huang, C. T. Chen,
H. C. Jeon, et al., *Appl. Phys. Lett.* **91**, 072507 (2007).
 - ¹⁰ S. Sonoda, S. Shimizu, T. Sasaki, Y. Yamamoto, and
H. Hori, *J. Cryst. Growth* **237**, 1358 (2002).
 - ¹¹ E. Sarigiannidou, F. Wilhelm, E. Monroy, R. M. Galera,
E. Bellet-Amalric, A. Rogalev, J. Goulon, J. Cibert, and
H. Mariette, *Phys. Rev. B* **74**, 041306(R) (2006).
 - ¹² K. W. Edmonds, S. V. Novikov, M. Sawicki, R. P. Cam-
pion, C. R. Staddon, A. D. Giddings, L. X. Zhao, K. Y.
Wang, T. Dietl, C. T. Foxon, et al., *Appl. Phys. Lett.* **86**,
152114 (2005).
 - ¹³ N. Nepal, M. O. Luen, J. M. Zavada, S. M. Bedair, P. Fra-
jtag, and N. A. El-Masry, *Appl. Phys. Lett.* **94**, 132505
(2009).
 - ¹⁴ N. Theodoropoulou, A. F. Hebard, M. E. Overberg, C. R.
Abernathy, S. J. Pearton, S. N. G. Chu, and R. G. Wilson,
Appl. Phys. Lett. **78**, 3475 (2001).
 - ¹⁵ M. Zajac, J. Gosk, E. Grzanka, M. Kamińska, A. Twar-
dowski, B. Strojek, T. Szyszko, and S. Podsiadło, *J. Appl.*
Phys. **93**, 4715 (2003).
 - ¹⁶ S. Dhar, O. Brandt, A. Trampert, K. J. Friedland, Y. J.
Sun, and K. H. Ploog, *Phys. Rev. B* **67**, 165205 (2003).
 - ¹⁷ S. Kuroda, N. Nishizawa, K. Takita, M. Mitome, Y. Bando,
K. Osuch, and T. Dietl, *Nature Mat.* **6**, 440 (2007).
 - ¹⁸ A. Bonanni, A. Navarro-Quezada, T. Li, M. Wegscheider,
Z. Matěj, V. Holý, R. T. Lechner, G. Bauer, M. Rovezzi,
F. D’Acapito, et al., *Phys. Rev. Lett.* **101**, 135502 (2008).
 - ¹⁹ M. J. Reed, F. E. Arkun, E. A. Berkman, N. A. Elmasry,
J. Zavada, M. O. Luen, M. L. Reed, and S. M. Bedair,
Appl. Phys. Lett. **86**, 102504 (2005).
 - ²⁰ M. H. Kane, M. Strassburg, W. E. Fenwick, A. Asghar,
A. M. Payne, S. Gupta, Q. Song, Z. J. Zhang, N. Dietz,
C. J. Summers, et al., *J. Crystal Growth* **287**, 591 (2006).
 - ²¹ G. Martinez-Criado, A. Somogyi, S. Ramos, J. Campo,
R. Tucoulou, M. Salome, J. Susini, M. Hermann, M. Eick-
hoff, and M. Stutzmann, *Appl. Phys. Lett.* **86**, 131927
(2005).
 - ²² J. A. Chan, J. Z. Liu, H. Raebiger, S. Lany, and A. Zunger,
Phys. Rev. B **78**, 184109 (2008).
 - ²³ A. Bonanni, *Semicond. Sci. Technol.* **22**, R41 (2007).
 - ²⁴ M.-H. Ham, S. Yoon, Y. Park, and J.-M. Myoung, *Appl.*
Surf. Sci. **252**, 6289 (2006).
 - ²⁵ X. Yang, Z. Chen, J. Wu, Y. Pan, Y. Zhang, Z. Yang,
T. Yu, and G. Zhang, *J. Cryst. Growth* **305**, 144 (2007).
 - ²⁶ A. Bonanni, D. Stifter, A. Montaigne-Ramil,
K. Schmidegg, K. Hingerl, and H. Sitter, *J. Cryst.*
Growth **248**, 211 (2003).
 - ²⁷ C. Simbrunner, M. Wegscheider, M. Quast, T. Li,
A. Navarro-Quezada, H. Sitter, A. Bonanni, and
R. Jakiela, *Appl. Phys. Lett.* **90**, 142108 (2007).
 - ²⁸ A. Bonanni, M. Kiecana, C. Simbrunner, T. Li, M. Sawicki,
M. Wegscheider, M. Quast, H. Przybylinska, A. Navarro-
Quezada, R. Jakiela, et al., *Phys. Rev. B* **75**, 125210
(2007).
 - ²⁹ S. Peters, T. Schmidtling, T. Trepk, U. W. Pohl, J.-T.
Zettler, and W. Richter, *J. Appl. Phys.* **88**, 4085 (2000).
 - ³⁰ M. Venkatesan, P. Stamenov, L. S. Dorneles, R. D. Gun-
ning, B. Bernoux, , and J. M. D. Coey, *Appl. Phys. Lett.*
90, 242508 (2007).
 - ³¹ M. Opel, K.-W. Nielsen, S. Bauer, S. Goennenwein,
J. Cezar, D. Schmeisser, J. Simon, W. Mader, and
R. Gross, *Eur. Phys. J. B* **63**, 437 (2008).
 - ³² A. Ney, M. Opel, T. C. Kaspar, V. Ney, K. Ollefs, T. Kam-
mermeier, S. Bauer, K.-W. Nielsen, S. T. B. Goennenwein,
M. H. Engelhard, et al., *New. J. Phys.* **12**, 013020 (2010).
 - ³³ F. D’Acapito, S. Colonna, S. Pascarelli, G. Antonioli,
A. Balerna, A. Bazzini, F. Boscherini, F. Campolungo,
G. Chini, G. Dalba, et al., *ESRF Newsletter* **30**, 42 (1998).
 - ³⁴ S. Pascarelli, F. Boscherini, F. D’Acapito, J. Hrdy,
C. Meneghini, and S. Mobilio, *J. Synchrotron Rad.* **3**, 147
(1996).
 - ³⁵ C. Maurizio, M. Rovezzi, F. Bardelli, H. G. Pais, and
F. D’Acapito, *Rev. Sci. Instrum.* **80**, 63904 (2009).
 - ³⁶ K. V. Klementev, *J. Phys. D: Appl. Phys.* **34**, 209 (2001).
 - ³⁷ M. Newville, *J. Synchrotron Rad.* **8**, 322 (2001).
 - ³⁸ B. Ravel and M. Newville, *J. Synchrotron Rad.* **12**, 537
(2005).
 - ³⁹ A. Ankudinov, B. Ravel, J. Rehr, and S. Conradson, *Phys.*
Rev. B **58**, 7565 (1998).
 - ⁴⁰ A. Poiarkova and J. Rehr, *Phys. Rev. B* **59**, 948 (1999).
 - ⁴¹ R. Passler, *J. Appl. Phys.* **101**, 093513 (2007).
 - ⁴² R. Salzer, D. Spemann, P. Esquinazi, R. Hohne, A. Setzer,
K. Schindler, H. Schmidt, and T. Butz, *J. Magn. Magn.*
Mat. **317**, 53 (2007).
 - ⁴³ A. Ney, T. Kammermeier, V. Ney, K. Ollefs, and S. Ye, *J.*
Magn. Magn. Mater. **320**, 3341 (2008).
 - ⁴⁴ *Using PPMS Superconducting Mag-
nets at Low Fields, Quantum Design,*
[http://www.qdusa.com/resources/pdf/ppmsappnotes/1070-
207.pdf](http://www.qdusa.com/resources/pdf/ppmsappnotes/1070-207.pdf) (2009).
 - ⁴⁵ M. Jamet, A. Barski, T. Devillers, V. Poydenot, R. Du-
jardin, P. Bayle-Guilmaud, J. Rotheman, E. Bellet-

- Amalric, A. Marty, J. Cibert, et al., *Nature Mat.* **5**, 653 (2006).
- ⁴⁶ G. Thaler, R. Frazier, B. Gila, J. Stapleton, M. Davidson, C. R. Abernathy, S. J. Pearton, and C. Segre, *Appl. Phys. Lett.* **84**, 1314 (2004).
- ⁴⁷ X. G. Cui, Z. K. Tao, R. Zhang, X. Li, X. Q. Xiu, Z. L. Xie, S. L. Gu, P. Han, Y. Shi, and Y. D. Zheng, *Appl. Phys. Lett.* **92**, 152116 (2008).
- ⁴⁸ M. Moreno, A. Trampert, B. Jenichen, L. Doweritz, and K. H. Ploog, *J. Appl. Phys.* **92**, 4672 (2002).
- ⁴⁹ M. Tanaka, H. Shimizu, and M. Miyamura, *J. Cryst. Growth* **227-228**, 839 (2001).
- ⁵⁰ A. Navarro-Quezada, W. Stefanowicz, T. Li, B. Faina, M. Rovezzi, R. T. Lechner, T. Devillers, F. d'Acapito, G. Bauer, M. Sawicki, et al., arXiv:1001.5418v1 (2010).
- ⁵¹ P. A. Lee, P. H. Citrin, P. Eisenberger, and B. M. Kincaid, *Rev. Mod. Phys.* **53**, 769 (1981).
- ⁵² F. Boscherini, in *Characterization of Semiconductor Heterostructures and Nanostructures*, edited by C. Lamberti (Elsevier, 2008), chap. 9, pp. 289–330.
- ⁵³ Y. L. Soo, G. Kioseoglou, S. Kim, S. Huang, Y. H. Kao, S. Kuwabara, S. Owa, T. Kondo, and H. Munekata, *Appl. Phys. Lett.* **79**, 3926 (2001).
- ⁵⁴ M. Sato, H. Tanida, K. Kato, T. Sasaki, Y. Yamamoto, S. Sonoda, S. Shimizu, and H. Hori, *Jpn. J. Appl. Phys.* **41**, 4513 (2002).
- ⁵⁵ X. Biquard, O. Proux, J. Cibert, D. Ferrand, H. Mariette, R. Giraud, and B. Barbara, *J. Supercond.* **16**, 127 (2003).
- ⁵⁶ R. Bacewicz, *J. Phys. Chem. Solids* **64**, 1469 (2003).
- ⁵⁷ M. Rovezzi, F. D'Acapito, A. Navarro-Quezada, B. Faina, T. Li, A. Bonanni, F. Filippone, A. A. Bonapasta, and T. Dietl, *Phys. Rev. B* **79**, 195209 (2009).
- ⁵⁸ R. Giraud, S. Kuroda, S. Marcet, E. Bellet-Amalric, X. Biquard, B. Barbara, D. Fruchart, D. Ferrand, J. Cibert, and H. Mariette, *Europhys. Lett.* **65**, 553 (2004).
- ⁵⁹ A. Stroppa and G. Kresse, *Phys. Rev. B* **79**, 201201 (2009).
- ⁶⁰ T. Yamamoto, *X-Ray Spectrom.* **37**, 572 (2008).
- ⁶¹ A. Titov, X. Biquard, D. Halley, S. Kuroda, E. Bellet-Amalric, H. Mariette, J. Cibert, A. E. Merad, G. Merad, M. B. Kanoun, et al., *Phys. Rev. B* **72**, 115209 (2005).
- ⁶² O. Sancho-Juan, A. Cantarero, N. Garro, A. Cros, G. Martínez-Criado, M. Salomé, J. Susini, D. Olgúin, and S. Dhar, *J. Phys.: Condens. Matter* **21**, 295801 (2009).
- ⁶³ F. Farges, *Phys. Rev. B* **71**, 155109 (2005).
- ⁶⁴ V. N. Antonov, A. N. Yaresko, and O. Jepsen, *Phys. Rev. B* **81**, 075209 (2010).
- ⁶⁵ R. Korotkov, *Physica B* **308-310**, 30 (2001).
- ⁶⁶ A. Wołoś, M. Palczewska, M. Zajac, J. Gosk, M. Kaminska, A. Twardowski, M. Bockowski, I. Grzegory, and S. Porowski, *Phys. Rev. B* **69**, 115210 (2004).
- ⁶⁷ J. Zenneck, T. Niermann, D. Mai, M. Röver, M. Kocan, J. Malindretos, M. Seibt, A. Rizzi, N. Kaluza, and H. Hardtdegen, *J. Appl. Phys.* **101**, 063504 (2007).
- ⁶⁸ A. Titov, Phd, Université Joseph-Fourier - Grenoble I (2006).
- ⁶⁹ Y. Joly, *Phys. Rev. B* **63**, 125120 (2001).
- ⁷⁰ Y. Joly, O. Bunu, J. E. Lorenzo, R. M. Galéra, S. Grenier, and B. Thompson, *Journal of Physics: Conference Series* **190**, 012007 (2009).
- ⁷¹ T. Graf, M. Gjukic, M. S. Brandt, M. Stutzmann, and O. Ambacher, *Appl. Phys. Lett.* **81**, 5159 (2002).
- ⁷² T. Graf, S. T. B. Goennenwein, and M. S. Brandt, *Phys. Status Solidi B* **239**, 277 (2003).
- ⁷³ M. Zajac, J. Gosk, M. Kamińska, A. Twardowski, T. Szyszko, and S. Podsiadlo, *Appl. Phys. Lett.* **79**, 2432 (2001).
- ⁷⁴ P. Bogusławski and J. Bernholc, *Phys. Rev. B* **72**, 115208 (2005).
- ⁷⁵ X. Y. Cui, B. Delley, A. J. Freeman, and C. Stampfl, *Phys. Rev. B* **76**, 045201 (2007).
- ⁷⁶ S. Marcet, W. Pacuski, E. Sarigiannidou, F. Wilhelm, D. Ferrand, S. Kuroda, R. M. Galera, E. Gheeraert, J. Cibert, A. Rogalev, et al., *phys. status solidi (c)* **3**, 4062 (2006).
- ⁷⁷ J. T. Vallin, G. A. Slack, S. Roberts, and A. E. Hughes, *Phys. Rev. B* **2**, 4313 (1970).
- ⁷⁸ J. T. Vallin and G. D. Watkins, *Phys. Rev. B* **9**, 2051 (1974).
- ⁷⁹ J. Gosk, M. Zajac, A. Wolos, M. Kaminska, A. Twardowski, I. Grzegory, M. Bockowski, and S. Porowski, *Phys. Rev. B* **71**, 094432 (2005).
- ⁸⁰ A. Wołoś, A. Wymolek, M. Kaminska, A. Twardowski, M. Bockowski, I. Grzegory, S. Porowski, and M. Potemski, *Phys. Rev. B* **70**, 245202 (2004).
- ⁸¹ T. Dietl, *Phys. Rev. B* **77**, 085208 (2008).
- ⁸² K. A. Kikoin and V. N. Fleurov, *Transition Metal Impurities in Semiconductors* (World Scientific, 2004).
- ⁸³ Y. S. Cho, H. Hardtdegen, N. Kaluza, M. von der Ahe, U. Breuer, H.-P. Boehm, P. Ruteranac, K. Schmalbuch, D. Wenzel, T. Schäpers, et al., *J. Cryst. Growth* **312**, 1 (2009).